



# The nonlinear dynamic analysis of elasto-plastic behaviour of the single-curved FGM shells under impact load

M. Shahraki<sup>1</sup>, F. Shahabian<sup>1,\*</sup>, M. Koohestani<sup>1</sup>

<sup>1</sup>Faculty of Engineering, Ferdowsi University of Mashhad, Mashhad, Iran

**ABSTRACT:** Functionally graded materials (FGM) are some kind of composite materials that due to the continuity of mixture of constituent materials, have more effective mechanical properties than composites which leads to eliminating interlayer stress concentration. The most application of these materials is in thin structures such as plates and shells. This research presents a Tamura-Tomota-Ozawa based model to obtain the elastoplastic behavior of Functionality graded materials under impact loads. Also, based on this model, the ceramic phase of FGM was considered as an isotropic elastic material and the metal phase was considered as an elastoplastic material. Several parametric studies have been conducted to assess different aspects of such material behavior. The results show that the maximum displacement of the shell has increased by increasing the volume fraction index and the thickness ratio, and it has decreased by increasing the aspect ratio. It was also observed that the thickness ratio(32%), volume fraction index(30%), aspect ratios(23%) and shell curvature (16%) parameters affect the maximum displacement of the shell. The elasto-plastic response of FGM shells is similar to homogeneous shells and the TTO model can describe the mechanical behavior of FGM shells beyond the elastic range where the FGM response is mainly governed by the plastic region of the metal phase.

## Review History:

Received: Nov. 15, 2019

Revised: Jan. 28, 2020

Accepted: Jan. 30, 2020

Available Online: Feb. 02, 2020

## Keywords:

Functionally Graded material

Single Curved Shells

Elasto-plastic Behavior

Nonlinear Dynamics

Impact Loading.

## 1- Introduction

Functionally graded materials are new and advanced materials with nonhomogeneous structures. The mechanical properties of these materials vary smoothly and continuously from one surface to another, and these changes are caused by a smooth change in the volume fraction of their constituent materials.

Functionally graded materials are usually made of ceramic and metal materials. Because; the structural material of the ceramic has low heat transfer coefficient and high resistance to temperature, which can withstand high heat, and on the other hand, another structural material, ie metal, provides the flexibility required. It is noteworthy that due to continuous changes in mechanical properties, the discontinuity problems which exist in composite structures are not created in functionally graded materials. In Fig. 1, the schematic view of a functionally graded material consists of two materials A and B is shown [1].

Christy et al. [2] Studied the static and dynamic behavior of thin plate by the Applied Element Method (AEM). Ashok and Jeyaraj [3] investigated a finite element analysis of tapered laminated composite plates with ply drop-off has been carried out to study the static deflection and normal stress patterns developed under non-uniform heating. Bever and Duwez [4], provided functionally gradient materials that their mechanical properties in local coordinate directions change

with a specific slope. Based on this theory, a national research on functionally graded materials began in 1984, looking for a way to produce heat-resistant materials at the Japan National Aerospace Laboratory by Kozumi et al. [5], and by providing a spherical FGM shell for the tip of the rocket in 1992 was completed.

Shahraki et al. [6] analyzed the effective parameters on the free vibrations of Functionally Graded plates with opening and stiffener. Sridhar and Prasad [7] conducted the experimental investigation on functionally graded reinforced concrete (FGRC) beams using hybrid fiber engineered cementitious composites (HYFECC). Horgan and Chan [8] obtained the equations of a hollow FGM cylinder in a plane strain state with a power-law distribution of elastic modulus in the radial direction using lame equations and the distribution of stress. Shahraki et al. [9] concerns about the effect of opening and stiffener on the geometric nonlinear dynamical behavior of single-curved FGM shells under the blast loads.

Analysis of elastoplastic FG structures has been drawn considerable attention from researchers in recent years. In this line of works, a composite model proposed by Tamura et al. [10] is widely adopted in evaluating the effective elastoplastic properties of FGM. Nie and Zhong [11] derived the solutions for stress distribution of curved elastoplastic FG beams subjected to pure bending. As far as the elastoplastic constitutive model was concerned, Tamura et al. [12] defined the rule of mixtures for metal alloy named TTO model, which

\*Corresponding author's email: shahabf@um.ac.ir



was extended to ceramic/metal system by Bocciarelli [13] to describe the elastoplastic behaviors of FGMs. Meanwhile, an inverse analysis procedure based on indentation tests was proposed by Nakamura et al. [14] to identify the constitutive parameters of FGMs. With this model, some literature were reported concerning thermal stress responses [15, 16] and fracture performances of FGMs [17, 18] Qiang et al. [19] concerns an elastic–plastic cohesive zone model for metal–ceramic interfaces and the corresponding nonlinear finite element implementation for general boundary value problems that accounts for nonlinear traction separation constitutive relation including fine-scale mechanisms of the bonded interfaces failure.

In this paper, mechanical properties of FGM material in two elastic and plastic regions were obtained. Modeling and Verification of the model were performed then the mechanical and geometrical properties of the single curved shell were investigated and their influence on the response of the shell was calculated. It was observed that the ratio of thickness and curvature had the greatest and least effect on the response, respectively.

## 2- Basics and concepts

The Cartesian coordinate system (x, y, z) of the single curved FGM shell can be located at the mid-surface or top of the shell. The z-axis is along with the shell's thickness and down in the z-direction is considered to be positive, and the y-axis is positioned along the length of the shell and perpendicular to the x-axis (Fig. 2). The shell displacement along the thickness direction is indicated by w.

According to Fig. 2, the volume fraction of ceramic material is as follows

$$V_c = \left(\frac{z + \alpha}{h}\right)^n \quad (1)$$

In Eq. (1), n is the volume fraction index, h is the shell thickness and  $\alpha$  is the distance of the center coordinates from the upper surface of the shell. For example, if the location of the coordinates is on the upper [20] or on the center [21] surface of the shell, the value of  $\alpha$  is zero and 0.5h, respectively. In this study, the value of  $\alpha$  is considered to be 0.5h.

### 2.1. Effective material properties

Based on Eq. (4), the constituent materials of the shell vary smoothly along with the thickness in such a way that the inner surface is metal-rich and the outer surface is ceramic-rich.

$$V_c(z) = \left(\frac{2z + h}{2h}\right)^n \quad (2)$$

$$V_m(z) = 1 - V_c(z) \quad (3)$$

Where  $V_c$  and  $V_m$  are the volume fractions of ceramic and metal constituents, respectively, the material properties of the FGM shell varies in the thickness direction (z) and, according to equation (4), it can be determined by a function of volume fraction of the constituent materials [22].

$$P = P_c V_c(z) + P_m V_m(z) \quad (4)$$

Where the subscripts m and c stand for the metal and ceramic constituents, respectively. From Eqs. (5), (6) and (7), for a single curved FGM shell, the modulus of elasticity E, the Poisson ratio  $\nu$ , and the mass density  $\rho$ , vary in thickness and can be expressed as

$$E = E_m + (E_c - E_m) \left(\frac{2z + h}{2h}\right)^n \quad (5)$$

$$\nu = \nu_m + (\nu_c - \nu_m) \left(\frac{2z + h}{2h}\right)^n \quad (6)$$

$$\rho = \rho_m + (\rho_c - \rho_m) \left(\frac{2z + h}{2h}\right)^n \quad (7)$$

In this study, 9 different values of the volume fraction index,  $n = 0.0, 0.2, 0.33, 0.5, 1.0, 2.0, 3.0, 5.0, \infty$  are considered for the analysis [23]. The values of  $n = 0$  and  $n = \infty$  correspond to ceramic-rich and metal-rich shells, respectively. The variation of the volume fraction index  $(z/h + 0.5)^n$ , in the thickness direction for various values of n, is shown in Fig. 3.

### 2.2. Plastic behaviour of the FGMs

The linear elastic response of FGMs obeys Hooke's law and their elastic properties evaluated approximately by micromechanics models for conventional composites (section 2.1). However, the elastoplastic behavior of metal/ceramic FGMs can be described by using the intermediate law of mixture, adapted for FGMs by Williamson et al. [24]. According to the TTO model, each layer in the FGM shell is treated as an isotropic composite for which the uniaxial stress  $\sigma$  and strain  $\varepsilon$  are related to the average uniaxial stresses  $\sigma_m$  and  $\sigma_c$  and strains  $\varepsilon_m$  and  $\varepsilon_c$  of the constituent materials.

$$\sigma = V_c \sigma_c + V_m \sigma_m \quad (8)$$

$$\varepsilon = V_c \varepsilon_c + V_m \varepsilon_m \quad (9)$$

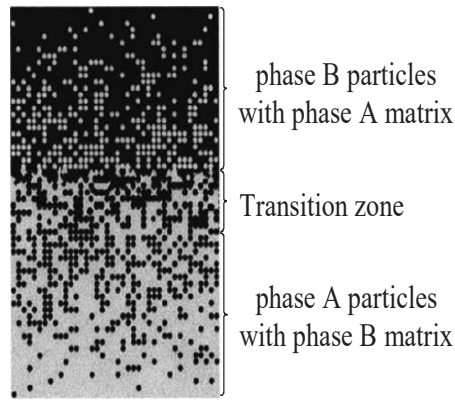


Fig. 1. Schematic representation of FGM composed of two phases A and B [1].

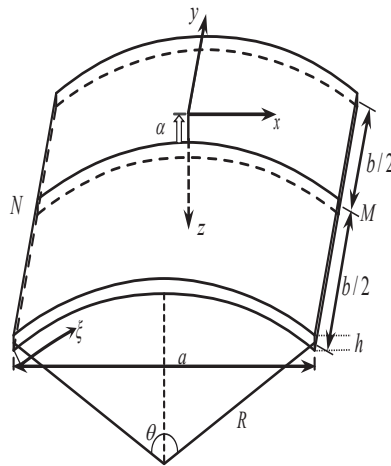


Fig. 2. Schematic of the single curved FGM shell and coordinate position.

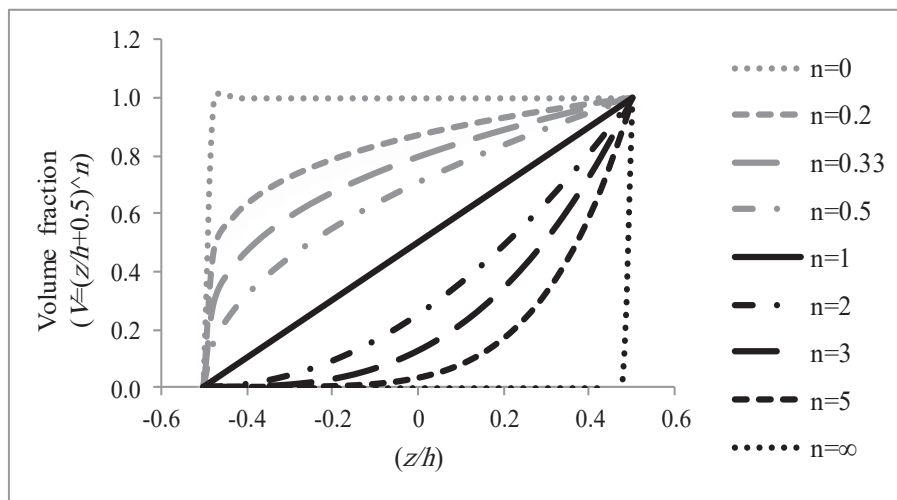


Fig. 3. Distribution of the volume fraction  $(z/h + 0.5)^n$  ..

The TTO model introduces an additional parameter  $q$  as follows

$$q = \frac{\sigma_c - \sigma_m}{|\varepsilon_c - \varepsilon_m|}, \quad 0 < q < \infty \quad (10)$$

The parameter  $q$  is the ratio of stress to strain transfer between two phases. The value of  $q$  depends on the constituent material properties and the microstructural interaction in the FGM. For example, the constituent elements have the equal stress distribution for  $q$  of 0 and the equal strain distribution for  $q$  of  $+\infty$ , respectively. Since the appropriate value of  $q$  depends on the type of base materials, it should be determined numerically or/and experimentally. For example, a value of  $q=91.6$  GPa,  $q=4.5$  GPa has been used for an Al/SiC FGM [25], and for a TiB/Ti FGM [18], respectively. For applications involving plastic deformation of ceramic/metal FGM, the TTO model assumes that the composite yields once the metal constituent yields. Accordingly, the yield stress  $\sigma_Y$ , of the composite may be obtained as follows

$$\sigma_Y(V_m) = \sigma_0 \left[ V_m + \frac{q + E_m}{q + E_c} \frac{E_c}{E_m} (1 - V_m) \right] \quad (11)$$

Where  $\sigma_0$  denotes the yield stress of the metal phase. The above equation indicates that the yield stress of the composite depends on the yield stress of metal, the volume fraction of the metal, Young's modulus of the constituent phases, and the parameter  $q$ . The following parametric equations determine the stress-strain ( $\sigma - \varepsilon$ ) curve for the FGM.

$$\frac{\varepsilon}{\varepsilon_Y} = \frac{V_c E}{q + E_c} \frac{\sigma_m}{\sigma_Y} + \frac{(q + V_m E_c) E}{(q + E_c) E_m} \frac{\sigma_0}{\sigma_Y} \left( \frac{\sigma_m}{\sigma_0} \right)^{n_0} \quad (12)$$

$$\frac{\sigma}{\sigma_Y} = \frac{V_m q + E_c}{q + E_c} \frac{\sigma_m}{\sigma_Y} + \frac{V_c q E_c}{(q + E_c) E_m} \frac{\sigma_0}{\sigma_Y} \left( \frac{\sigma_m}{\sigma_0} \right)^{n_0} \quad (13)$$

Where  $\varepsilon_Y = \sigma_Y / E$  is the yield strain of the FGM and  $n_0$  is the hardening exponent of the metal. The least-squares method determines the hardening exponent of the metal using the equation

$$\varepsilon_m = \varepsilon_0 \left( \frac{\sigma_m}{\sigma_0} \right)^{n_0} \quad (14)$$

Where  $\varepsilon_0 = \sigma_0 / E_m$  is the yield strain of the metal. Fig. 4 shows the schematic of the stress-strain curve of the FGM described by the TTO model.

In order to evaluate of elasto-plastic behaviour of FGM, can use TiB / Ti (FGM) that studied by Jane et al. [18]. The metal and ceramic material properties used in FGM are given in Table 1 and the stress-strain curve of Titanium is shown in Fig. 5. The comparison of the obtained stress-strain curves of FGM are given in Fig. 6. There is a good agreement between the TTO model and research studies by Jane et al. [19].

### 3- Modeling procedure

In this work, the commercial finite element software CAE is used, and the method is explicit and dynamic to analyze single curved FGM shells under impact loading. The shells meshed with four-node shell elements [26]. For this purpose, a shell with  $a=b=1$  (Fig. 1) has been analyzed with a nonlinear dynamic response. The parameters of the shells including volume fraction index, thickness ratio, aspect ratio, and curvature were investigated. The type of the FGM is selected as ceramic-metal (Al-SiC). The mechanical properties of these materials such as Young's modulus, density, and Poisson ratio are given in Table 2 [20]. Also, the stress-strain curves of Al and SiC are shown in Fig. 7 [20].

#### 3.1. Determining the number of FGM shell layers

In this study, an equivalent homogenous laminated approach is used for modeling FGM shells. In the used approach, the thickness of the shells is divided into a finite number of homogenous layers and the equivalent effective material properties of these layers are defined of section 2 within the layer as [23];

$$P_{eq}^k = \int_{z^{b_K}}^{z^{t_K}} \frac{P(z)}{h_K} dz, \quad K = 1, 2, \dots, N \quad (15)$$

To determine the number of FGM layers, some convergence analysis for the FGM shell (Fig. 1) with  $R/a=4$ , volume fraction index  $n=1$ , thickness  $h=6$  mm and  $20 \times 20$  mm mesh size under impact load with maximum overpressure ( $P_0$ ) 50 kPa based on Eqs. (15), (16) and (17) were performed [23]. For the shell response to move out of the elastic zone into the plastic zone, we need a high implementation rate force. that impact load with  $P_0=1$  MPa by Friedlander function Eq. (18) can pass through the elastic zone and into the plastic zone. Figures 15, 18, 21, and 23 show that the response enters the plastic zone after some time. It is also seen in Fig. 26 that the stress and strain created in the shell under this load have passed the yield point of the FGM.

$$P(x, y, t) = P_0 P_t(t) P_s(x, y) \quad (16)$$

$$P_s(x, y) = 1.0 \quad (17)$$

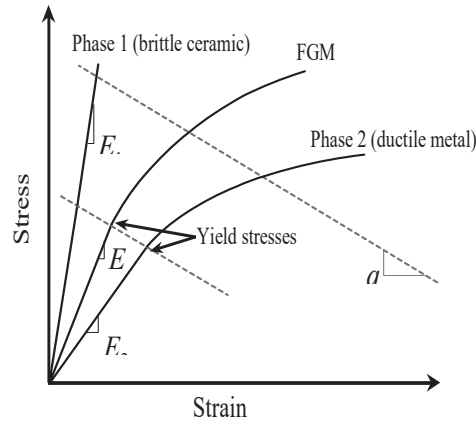


Fig. 4. Schematic of the stress–strain curve of the FGM based on TTO model [18].

Table 1. Ti and TiB material properties [18].

Materials	Young's modulus (GPa)	Poisson's ratio	Yield stress (MPa)	Hardening Exponent
Ti	107	0.34	450	14
TiB	375	0.14		

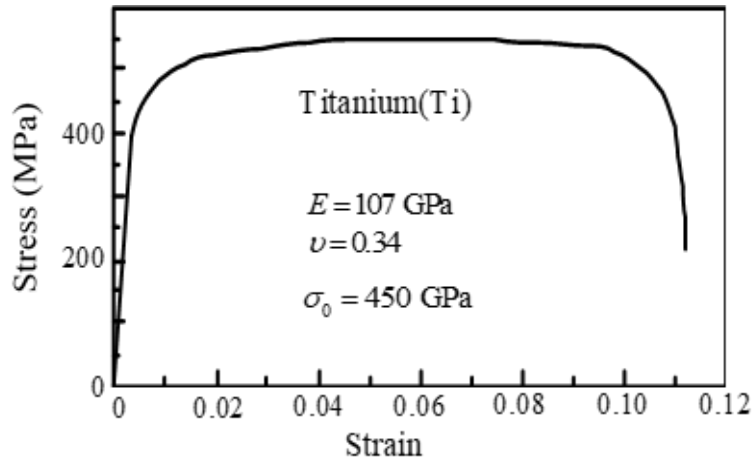


Fig. 5. Experimental stress-strain curve of Titanium [18].

$$\text{Step load: } \begin{cases} P_t(t) = 1, & t \leq t_p \\ = 0, & t > t_p \end{cases} \quad (18)$$

Friedlander Function :

$$\begin{cases} P_t(t) = (1 - t / t_p) e^{-\alpha t / t_p}, & t \leq t_p \\ = 0, & t > t_p \end{cases} \quad (19)$$

Where  $P_0$  is the maximum overpressure on the shell surface,  $P_s$  is the distribution of the load on the shell surface,  $P_t$  is the distribution of the load in the time domain,  $\alpha'$  is a waveform parameter,  $t$  is elapsed time and  $t_p$  is loading duration. In all analyses,  $t_p$  is considered as 20 ms and  $\alpha'$  is considered as 2 [23].

After analyzing the maximum central displacement, 14 layers were used as the appropriate state for the analysis of the FGM shell. The convergence analysis results for FGM are shown in Fig. 8.

Based on Section 2, the stress-strain curves of single curved FGM shells with 14 continuous layers for three volume fraction indexes,  $n=0.5, 1,$  and  $2$  are shown in Figs.9 to 11.

### 3.2. Meshing the FGM shell

In order to determine the mesh sizes, elements with various dimensions were used and the effects of the mesh sizes were investigated. Hence, in the single curved FGM shell

with a curvature of  $k=0.25$  (radius 4m), the thickness of  $h=6\text{mm}$ , volume fraction index  $n=1$ , under the impact load with  $P_0=50\text{ kPa}$  and uniformly distributed step load Eq. (17) and simple boundary condition, several convergence analyses were conducted. The obtained maximum displacements are shown in Fig. 12. As seen from Fig. 12,  $10 \times 10\text{ mm}$  mesh size are suitable for acceptable maximum displacement results. Fig. 13 shows the geometry and mesh of the FGM shell.

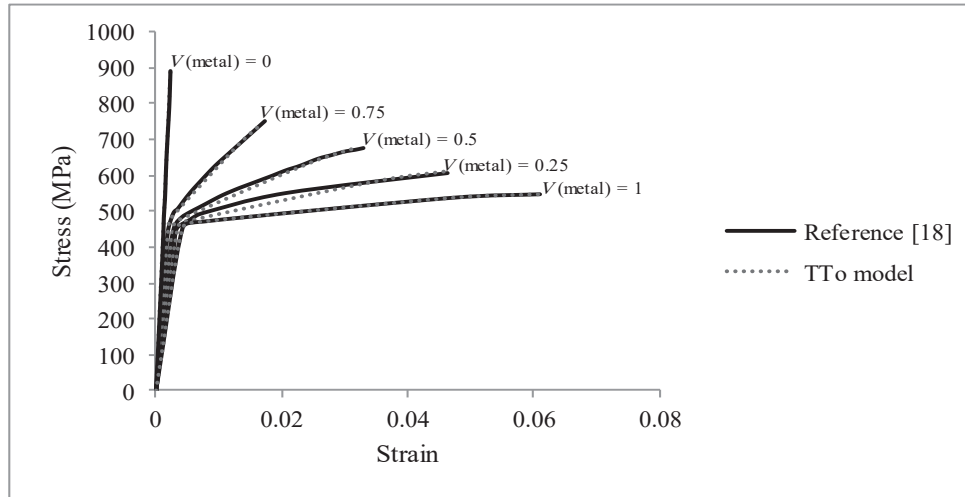


Fig. 6. Comparison of FGM stress-strain curves.

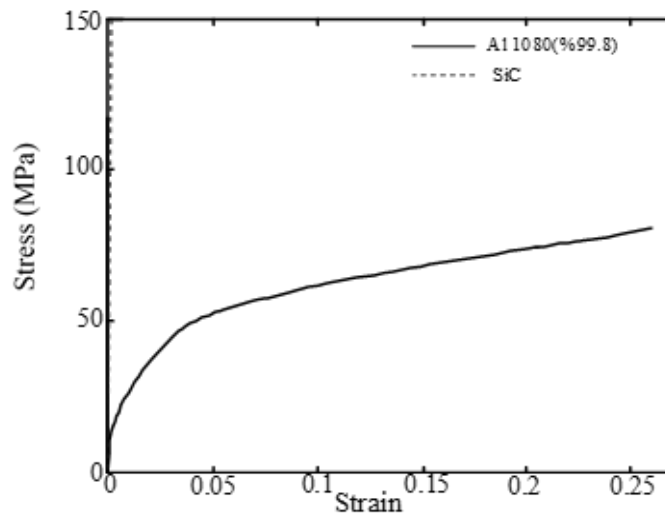


Fig. 7. The true stress-strain diagrams of Al and SiC phases [20].

Table 2. Mechanical properties of FGM shell constituent materials [20].

Materials	Young's modulus (GPa)	Poisson's ratio	Density (kg/m <sup>3</sup> )	Yield stress (MPa)	Hardening exponent
Al	67	0.33	2702	24	2
SiC	302	0.17	3100		

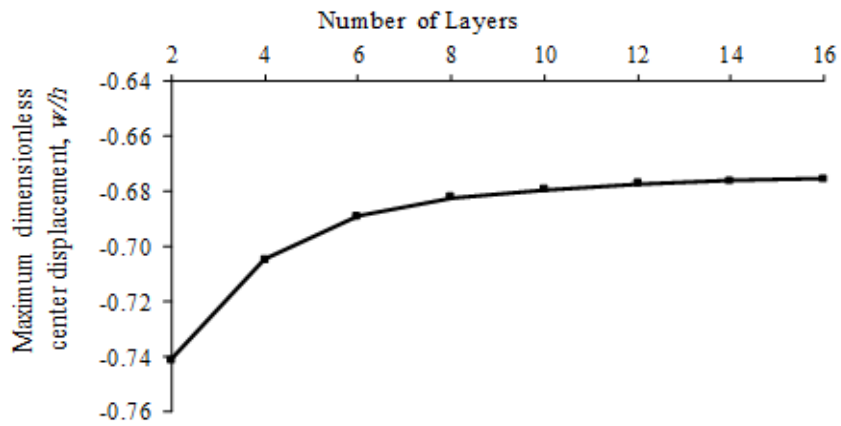


Fig. 8. Number of single curved FGM shell layers.

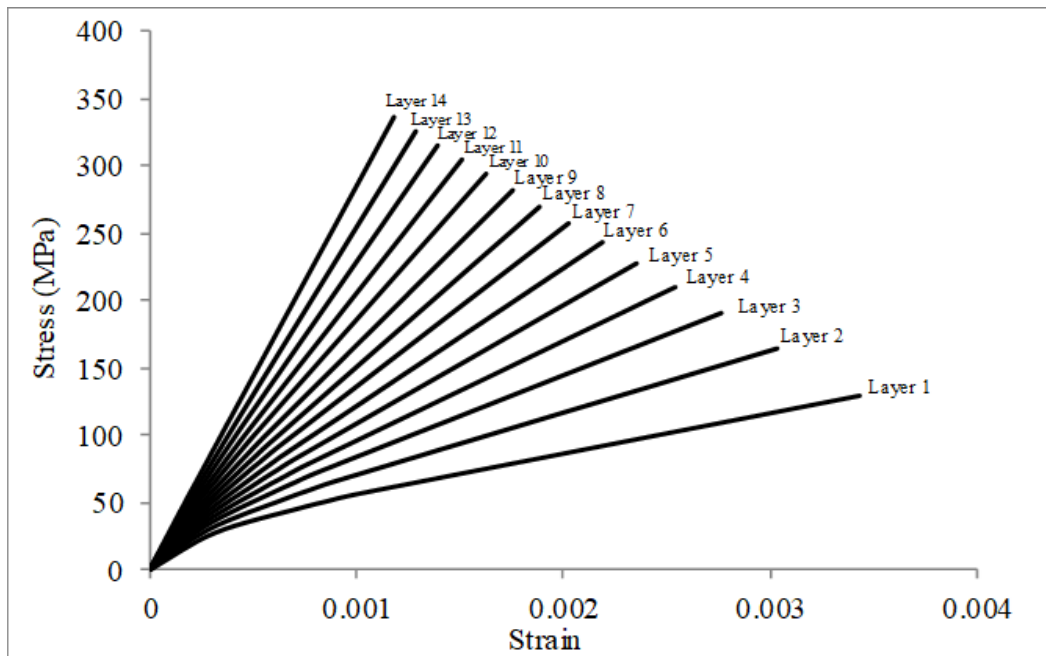


Fig. 9. The stress-strain curve of single curved FGM shell with 14 layers ( $n=0.5$ ).

Table 3. Material properties of FGM shell [27].

Materials	Young's modulus (GPa)	Density ( $\text{kg/m}^3$ )	Poisson's ratio
Titanium(Ti-6Al-4V)	105.6960	4429	0.2981
Zirconia ( $\text{ZrO}_2$ )	154.3211	5700	0.298

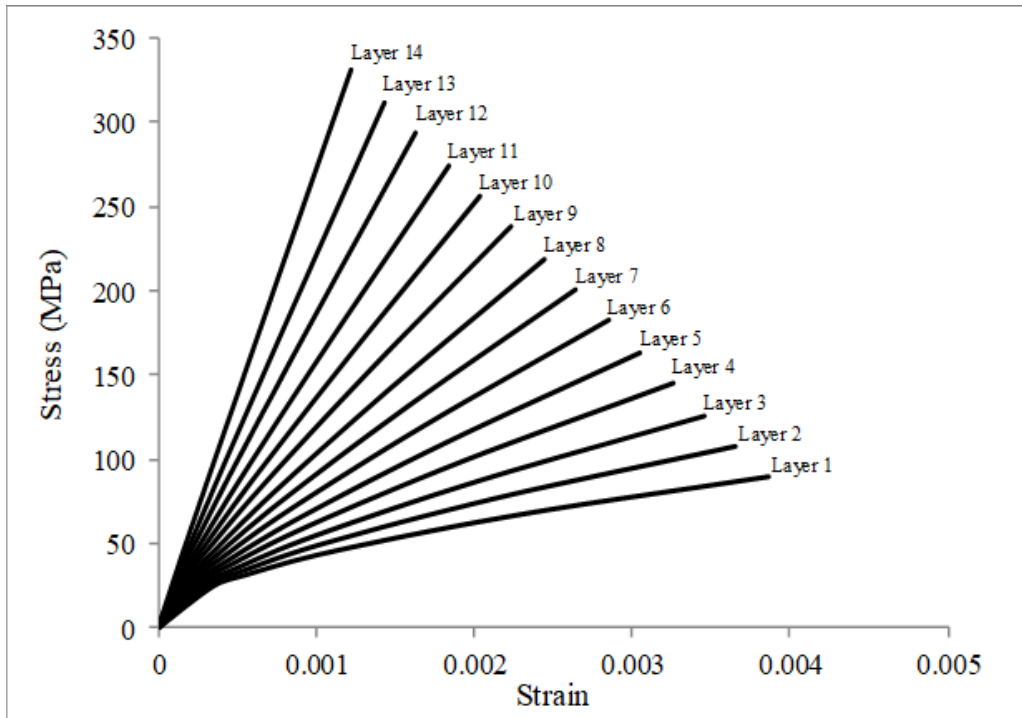


Fig. 10. The stress-strain curve of single curved FGM shell with 14 layers ( $n=1$ ).

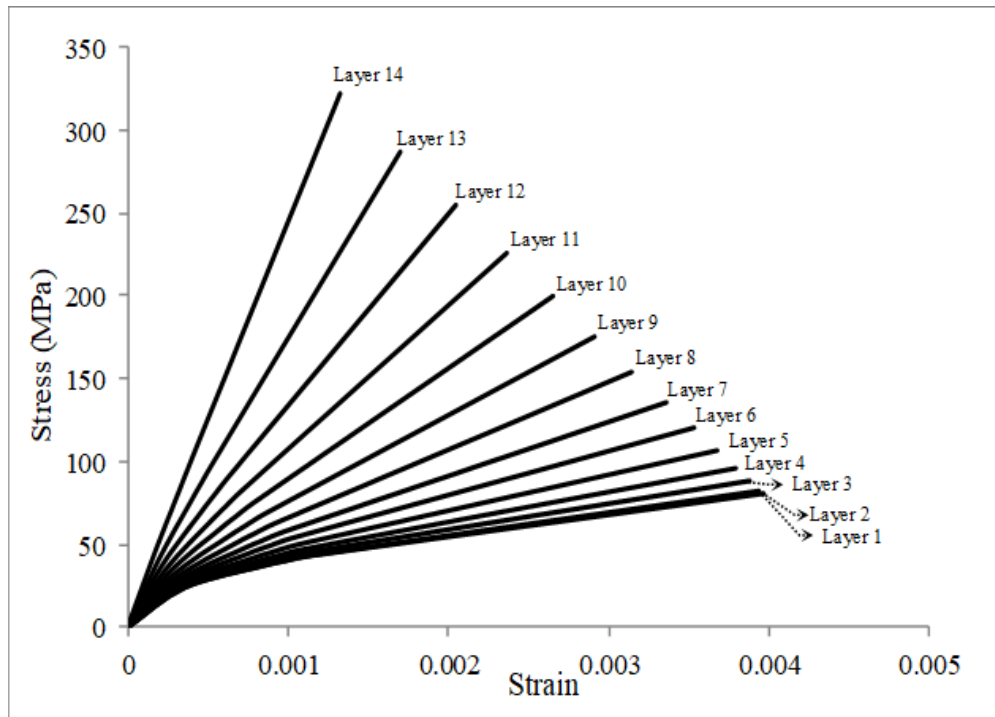


Fig. 11. The stress-strain curve of single curved FGM shell with 14 layers ( $n=2$ ).

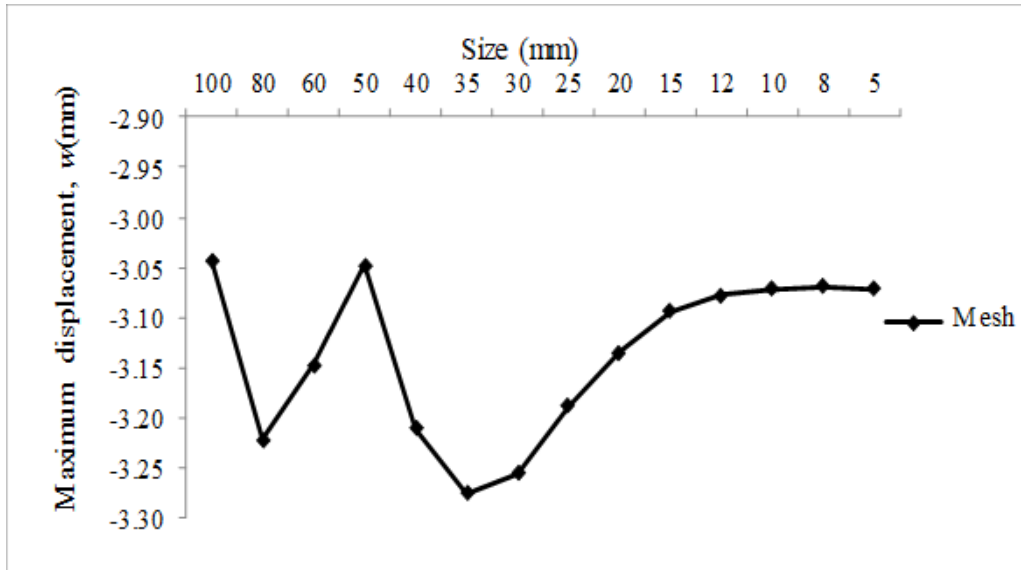


Fig. 12. Maximum displacement in convergence analyses of single curved FGM shell.

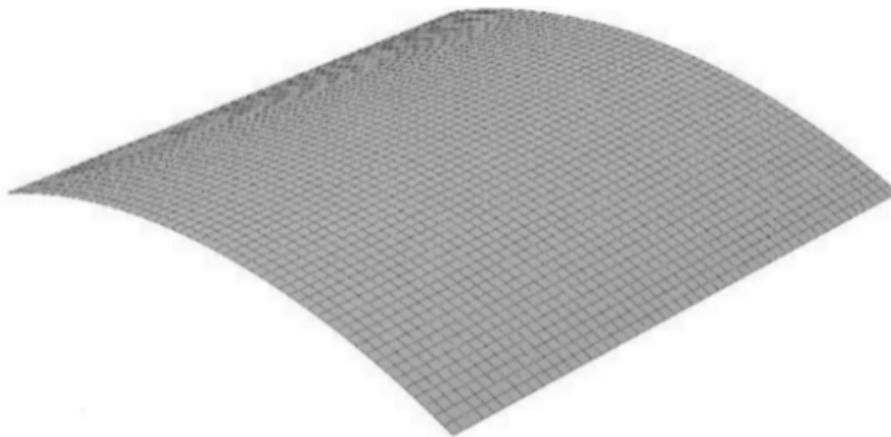


Fig. 13. Geometry and mesh of the single curved FGM shell.

#### 4- Validation of modeling

The validity of the analysis was considered by results provided by Hajului et al. [27]. They Reviewed the nonlinear dynamic response of FGM cylindrical shells under uniform pressure  $q(t) = 1500 \sin(600t)$ .

These shells are with the ratios of  $R/h = 500$ ,  $L/R = 80$  ( $R$  is the radius,  $h$  is the thickness and  $L$  is the length of the shell) and have simple support with two volume fraction indexes ( $n = 0, 2$ ). The properties of the materials are given in Table 3.

To verify this mechanism a finite element software, CAE (computer-aided engineering), has been utilized. The central displacement-time history is displayed in Fig. 14 and the maximum central displacement for the two volume fraction indexes is shown in Table 4. It can be seen that modeling results have an acceptable accuracy compared to the reported values obtained from the reference [27].

#### 5- Parametric studies

##### 5.1. Single curved FGM shell with various volume fraction index ( $n$ )

To investigate the effect of the volume fraction index, several single curved FGM shells with nine volume fraction index of  $n = 0.0, 0.2, 0.33, 0.5, 1.0, 2.0, 3.0, 5.0, \infty$ ,  $R/h=300$ ,  $R/a=4$ , and  $b/a=1$  under impact load with  $P_0=1$  MPa by The Friedlander function Eq. (18) have been analyzed. The maximum displacement-time history is displayed in Fig. 15. It is observed from Fig. 15 that by increasing the volume fraction index, the vibration amplitude and frequency of the FGM shell, decreased and increased, respectively. Also, as shown in Fig. 15, by increasing the volume fraction index, the maximum displacement increases; in such a way that the highest displacement occurs in the metal-rich shell ( $n = \infty$ ) and the least displacement occurs in the ceramic-rich shell ( $n = 0$ ).

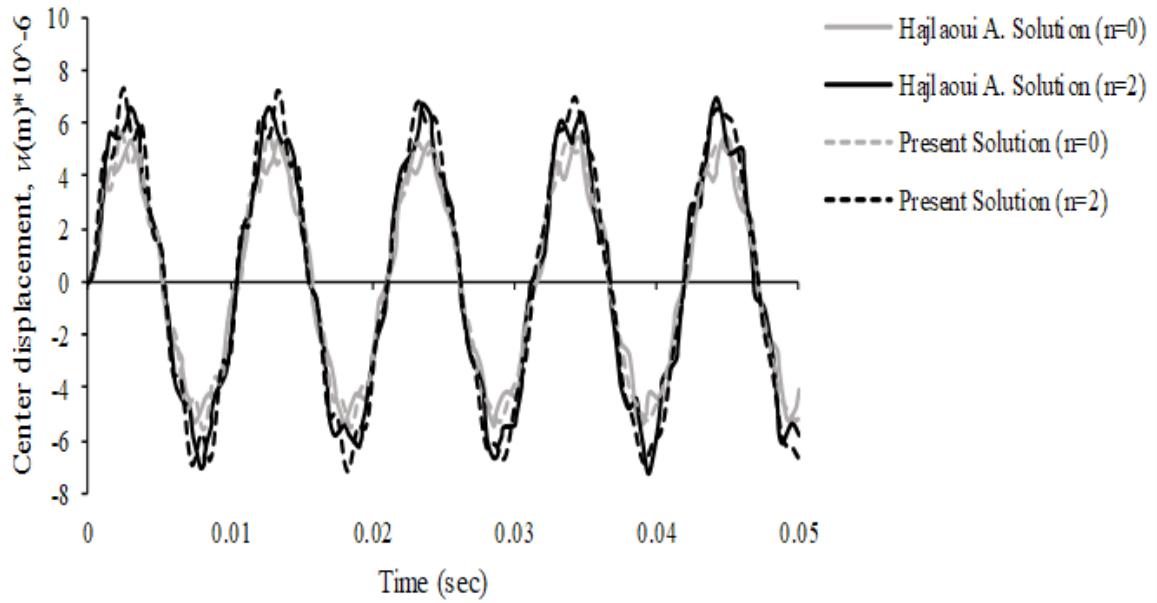


Fig. 14. Central displacement-time history of the FGM cylinder shell for the present solution and reference [27].

Table 4. Comparisons of results in the present solution and reference [27].

Volume fraction index	Present solution	Reference [29]	Difference (%)
0	-5.518	-5.458	1.09
2	-7.193	-7.204	-0.15

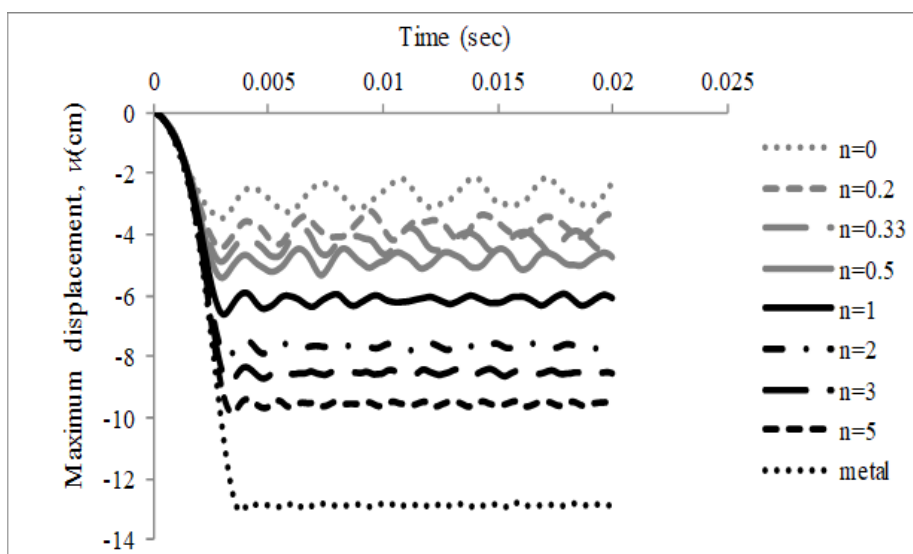


Fig. 15. Maximum displacement-time history of FGM shells with various volume fraction indexes.

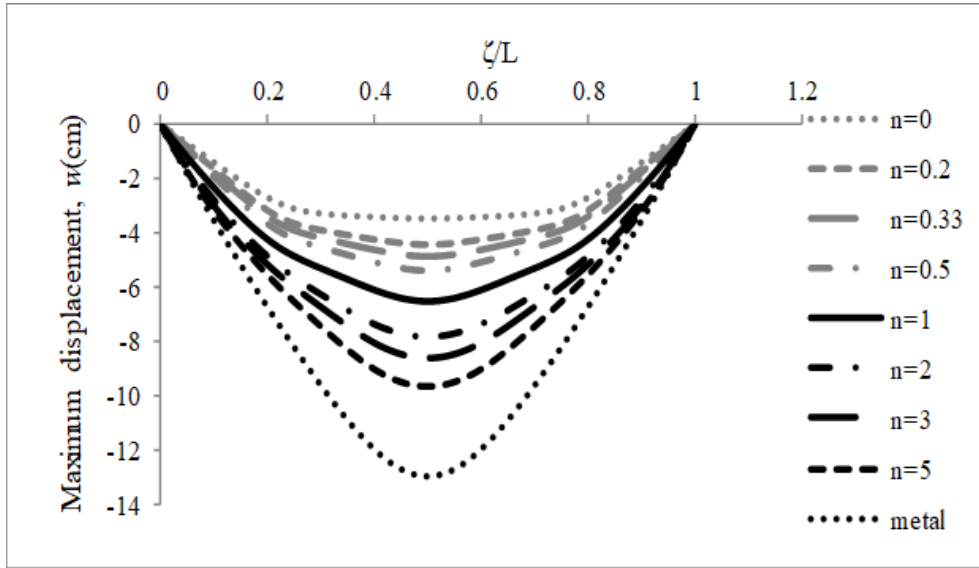


Fig. 16. Maximum displacement of the FGM shells with various volume fraction indexes on the MN path.

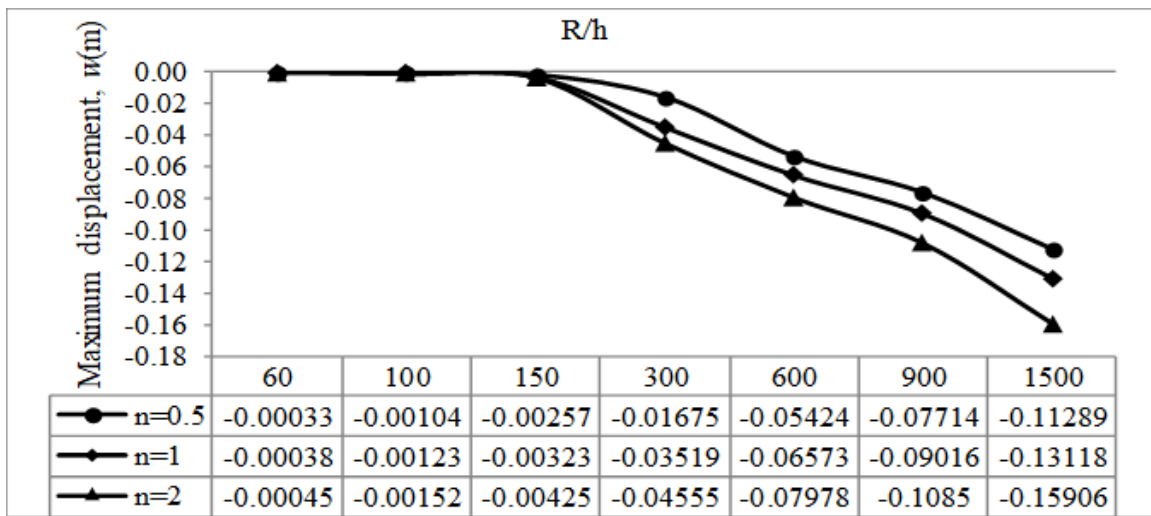


Fig. 17. Maximum displacement with different shell thicknesses and three volume fraction indexes.

The maximum displacements of the shell with different volume fraction indexes ( $n$ ) on the MN path (Fig. 2) are shown in Fig. 16. By varying the volume fraction index, the location of the maximum displacement of the shell changes; in such a way that by increasing the volume fraction index, the maximum displacement location moves toward the shell's center.

### 5.2. Single curved FGM shell with various thickness ratios ( $R/h$ )

To investigate the effect of shell thickness ratio, several single curved FGM shells with seven different thickness

ratios of  $R/h=60, 100, 150, 300, 600, 900, 1500$ ,  $b/a=1$ ,  $R/a=4$  and with three volume fraction indexes of  $n=0.5, 1$ , and  $2$  under impact load with  $P_0=1$  MPa by Friedlander function Eq. (18) have been analyzed. As shown in Fig. 17, the maximum displacement of the FGM shell has decreased by increasing the thickness ratio. Also, the maximum displacement-times history of FGM shells for  $n=2$  are shown in Fig. 18. It is observed that by increasing the  $R/h$  ratio, the vibration amplitude and frequency of the FGM shell, decreased and increased, respectively. The maximum displacements of

the shells for  $n=1$  with different thickness ratios ( $R/h$ ) on the MN path (Fig. 2) are shown in Figs. 19. It can be seen that by reducing the thickness ratio, the maximum displacement location moves toward the shell's center.

### 5.3. Single curved FGM shell with various aspect ratios ( $b/a$ )

In order to investigate the effect of shell aspect ratio ( $b/a$ ), several single curved FGM shells with seven aspect ratios of  $b/a=0.2, 0.33, 0.5, 1, 2, 3, 5$ ,  $R/h=300$ ,  $R/a=4$  and three volume fraction indexes of  $n=0.5, 1$  and  $2$  under impact load

with  $P_0=1$  MPa by Friedlander function Eq. (18) have been analyzed. As shown in Fig. 20, by increasing the aspect ratio, the maximum displacement of the FGM shell has increased at first and then remained almost constant. The maximum displacement-time history of FGM shell for  $n=2$  is shown in Fig. 21; Also, the maximum displacements of the shells for  $n=1$  with different aspect ratios ( $b/a$ ) on the MN path (Fig. 2) are shown in Figs 22. It can be seen that by increasing the aspect ratio, the maximum displacement location moves toward the shell's center.

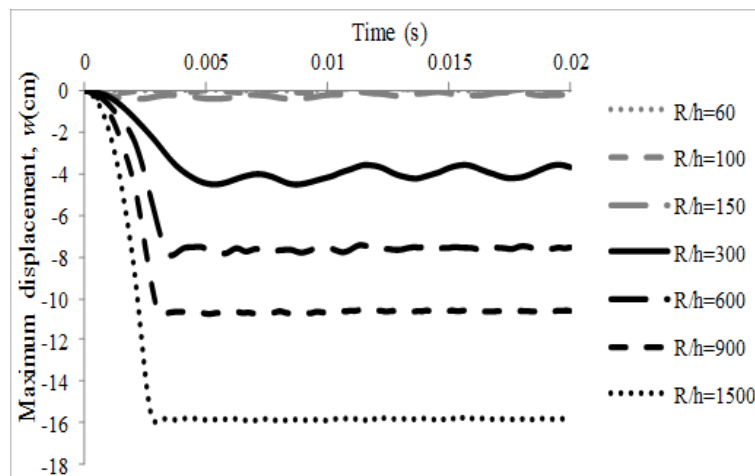


Fig. 18. Maximum displacement-time history of FGM shells with various thicknesses under impact load ( $n=2$ ).

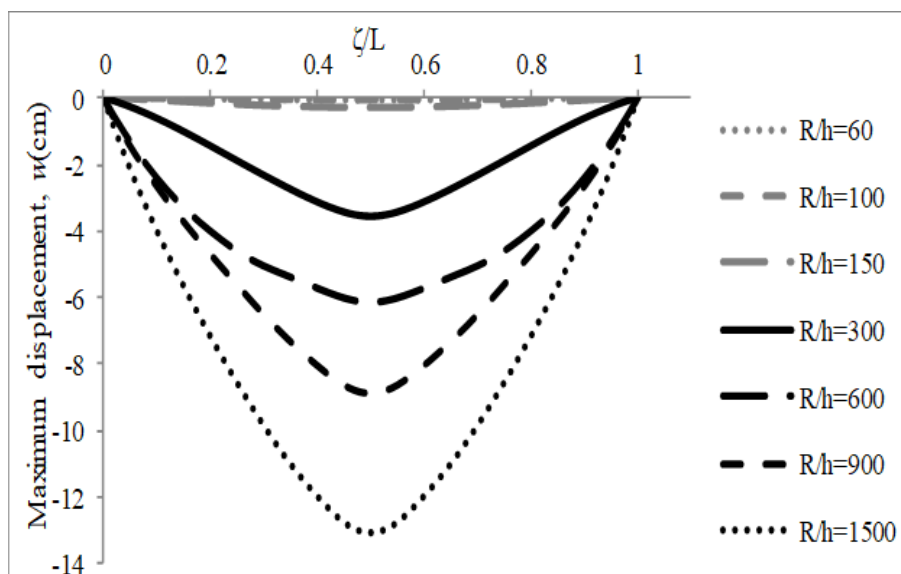


Fig. 19. Maximum displacement of the FGM shells with various thicknesses on the MN path ( $n=1$ ).

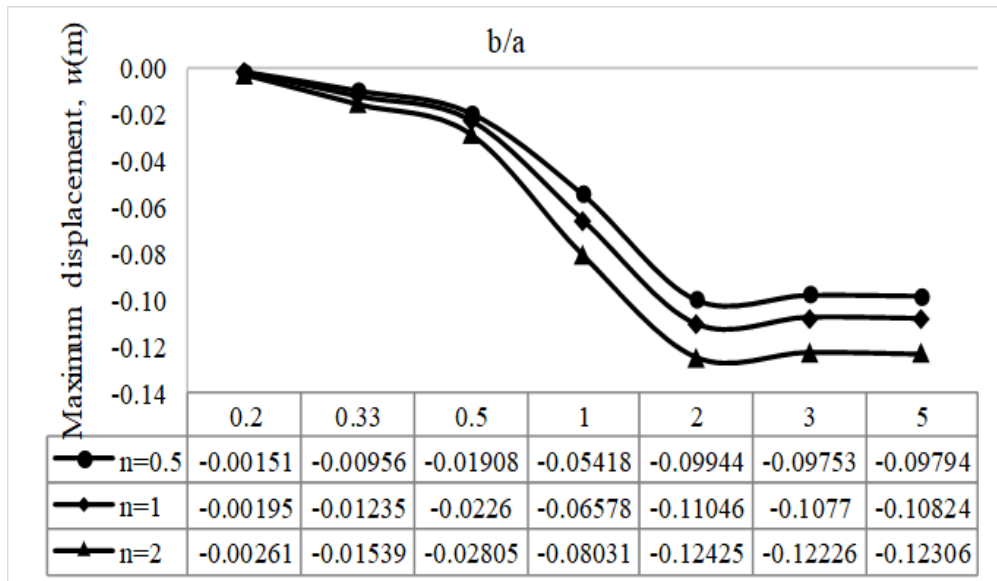


Fig. 20. Maximum displacement with different aspect ratios and three volume fraction indexes.

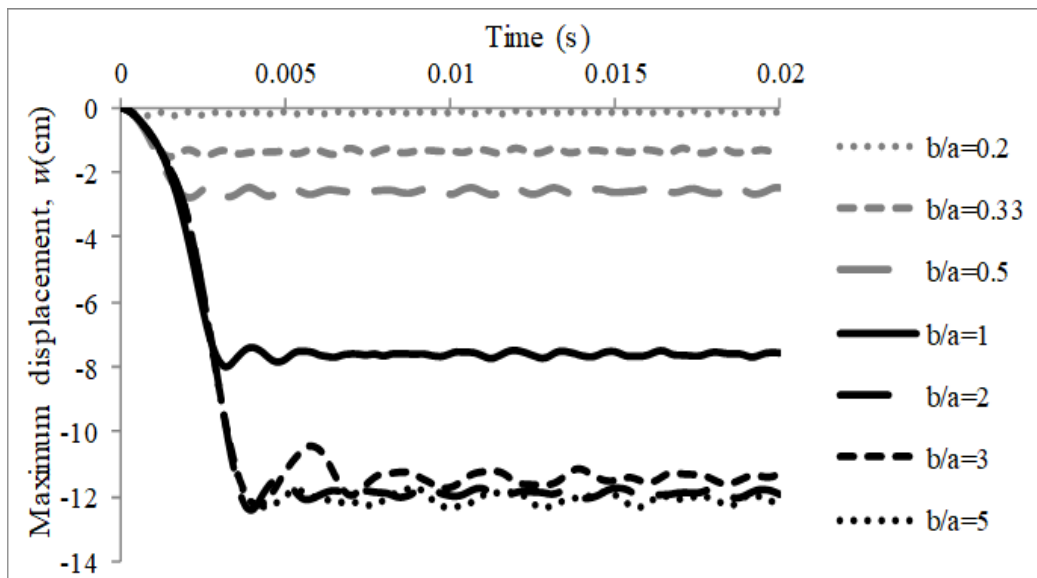


Fig. 21. Maximum displacement-time history of FGM shells with various aspect ratios under impact load ( $n=2$ ).

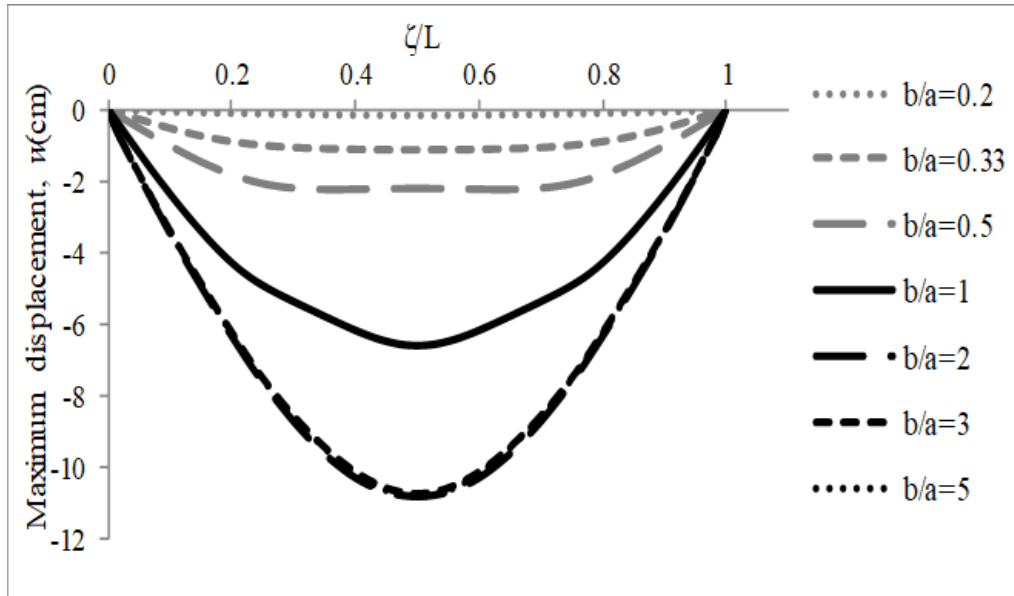


Fig. 22. Maximum displacement of the FGM shells with various aspect ratios on the MN path ( $n=1$ ).

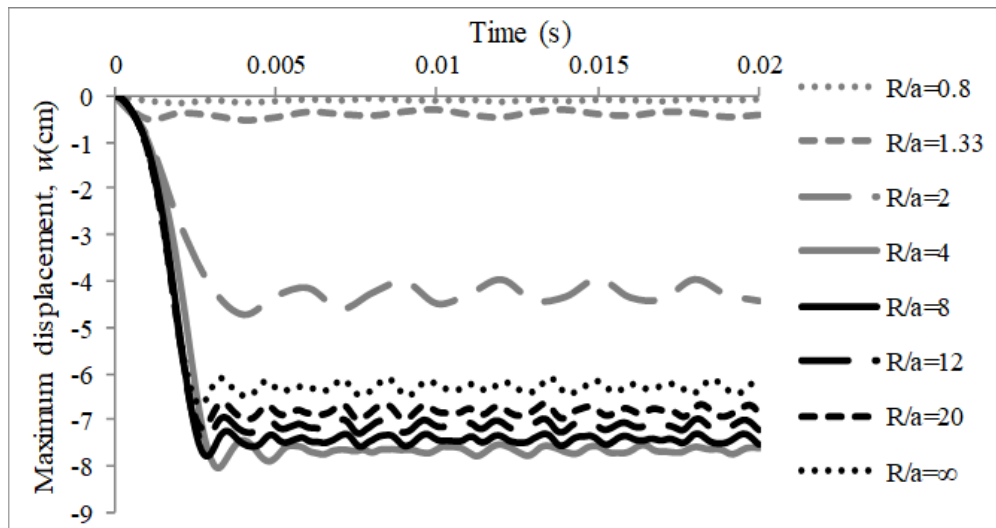


Fig. 23. Maximum displacement-time history of FGM shells with various curvatures under impact load ( $n=2$ ).

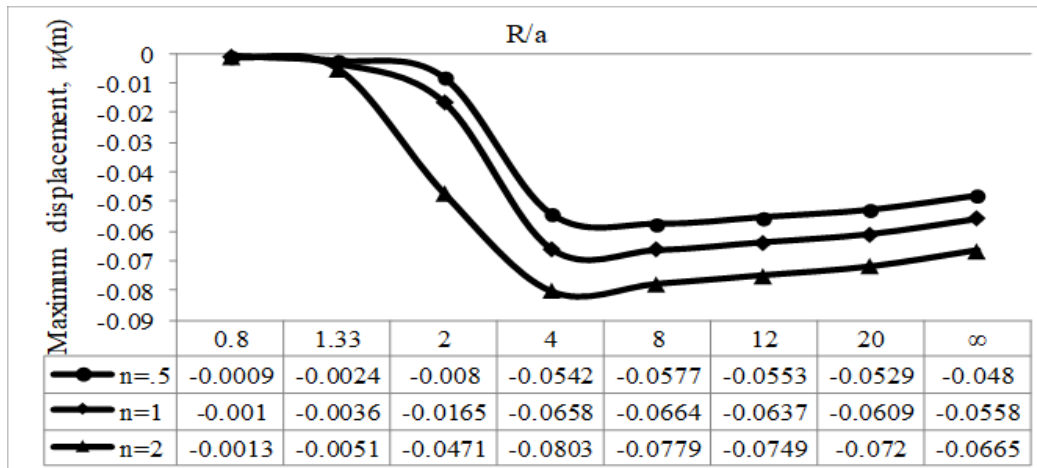


Fig. 24. Maximum displacement with various curvatures and three volume fraction indexes.

#### 5.4. Single curved FGM shell with various curvatures ( $\kappa$ )

In order to investigate the effect of curvature  $\kappa=1/R$ , several single curved FGM shells with eight curvature ratios of  $R/a=0.8, 1.33, 2, 4, 8, 12, 20, \infty$  (plan),  $R/h=300, b/a=1$  and three volume fraction indexes of  $n=0.5, 1$  and  $2$  under impact load with  $P_0=1$  MPa by Friedlander function Eq. (18) have been analyzed. The maximum displacement-times history of FGM shells for  $n=2$  are shown in Fig. 23. It can be seen in Fig. 24 that by increasing the ratio of  $R/a$ , the maximum displacements of the FGM shell has increased at first, and then it has decreased. For example, in FGM shells with  $n=0.5$  and  $1$ , the peak displacement occurs in  $R/a=8$ , and FGM shells with  $n=2$  the peak displacement occurs in  $R/a=4$ . Also, the maximum displacements of the shells for  $n=1$  with different curvatures ( $\kappa$ ) on the MN path (Fig. 2) are shown in Fig 25. It can be seen that by reducing the curvature, the maximum displacement location moves toward the shell's center.

#### 6- The stress-strain curve of the single curved FGM shell

The single curved FGM shells with  $R/h=300, b/a=1, R/a=4$ , and with three volume fraction indexes of  $n=0.5, 1$  and  $2$  under impact load with  $P_0=1$  MPa by Friedlander function Eq. (18) have been analyzed, And it has been observed that maximum displacement occurs in the center of the shell, so the stress-strain curve in the center of the FGM shell is examined, It can be seen from Fig. 26 that with increasing volume index the FGM shell yield point has increased but the slope of the stress-strain curve decreases.

#### 7- The effect of geometrical and mechanical parameters on the shell response

To determine the effect of each parameter ( $n, R/h, R/a, b/a$ ) on the maximum displacement of the single curved FGM shell, the coefficient of determination ( $r$ ) has been used, which indicates the strength of geometrical and mechanical variable effects on the shell response. For example, if  $r=0.75$ ,

it means that 75% of the changes in  $y$  can be explained by changes in the  $x$  parameter. The correlation coefficient ( $\hat{\rho}_{xy}$ ) can be determined by Substitution of the mean values ( $\bar{x}, \bar{y}$ ) using Eqs. (19) and (20) and the standard deviation ( $S_x, S_y$ ) using Eqs. (21) and (22) into Eq. (23). By using Eq. (24), the coefficient of determination ( $r$ ) can be determined [28].

$$\bar{x} = \frac{1}{m} \sum_{i=1}^m x_i \quad (20)$$

$$\bar{y} = \frac{1}{m} \sum_{i=1}^m y_i \quad (21)$$

$$S_x = \sqrt{\frac{\sum_{i=1}^m (x_i - \bar{x})^2}{m-1}} = \sqrt{\frac{(\sum_{i=1}^m x_i^2) - m(\bar{x})^2}{m-1}} \quad (22)$$

$$S_y = \sqrt{\frac{\sum_{i=1}^m (y_i - \bar{y})^2}{m-1}} = \sqrt{\frac{(\sum_{i=1}^m y_i^2) - m(\bar{y})^2}{m-1}} \quad (23)$$

$$\hat{\rho}_{xy} = \frac{1}{m-1} \frac{\sum_{i=1}^m (x_i - \bar{x})(y_i - \bar{y})}{S_x S_y} = \frac{1}{m-1} \frac{\sum_{i=1}^m (x_i y_i) - m \bar{x} \bar{y}}{S_x S_y} \quad (24)$$

$$r = \hat{\rho}_{xy}^2 \quad (25)$$

Where  $x_i$  is the effective parameter (volume fraction index, curvature, thickness ratio, and aspect ratio) on the maximum displacement of the shell ( $y$ ).

In these relationships,  $x$  can be substituted by each of the geometrical and mechanical parameters ( $n$ ,  $R/h$ ,  $R/a$ ,  $b/a$ ) that affect the maximum displacement of the FGM shell ( $y$ ).  $m$  is the number of models that were considered for each parameter. The maximum displacements of the FGM shells with

different values of mechanical and geometrical parameters were investigated in sections 4.3, 4.4, 4.5, and 4.6. According to Table 5, the effectiveness and coefficient of determination for each of the FGM shell parameters are shown. It can be seen that the  $R/h$  has the greatest effect on the maximum displacement of the single curved FGM shell. The effect of parameters relative to each other, on the maximum displacement of the FGM shell, is shown in Fig. 27.

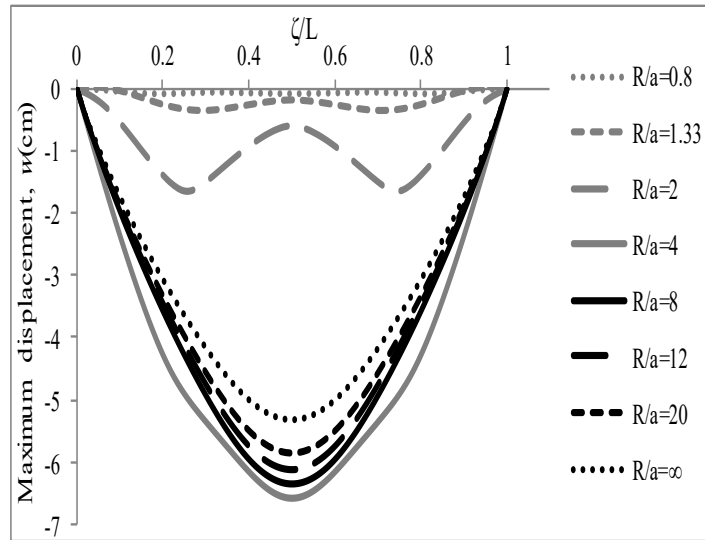


Fig. 25. Maximum displacement of the shells with various curvatures on the MN path ( $n=1$ ).

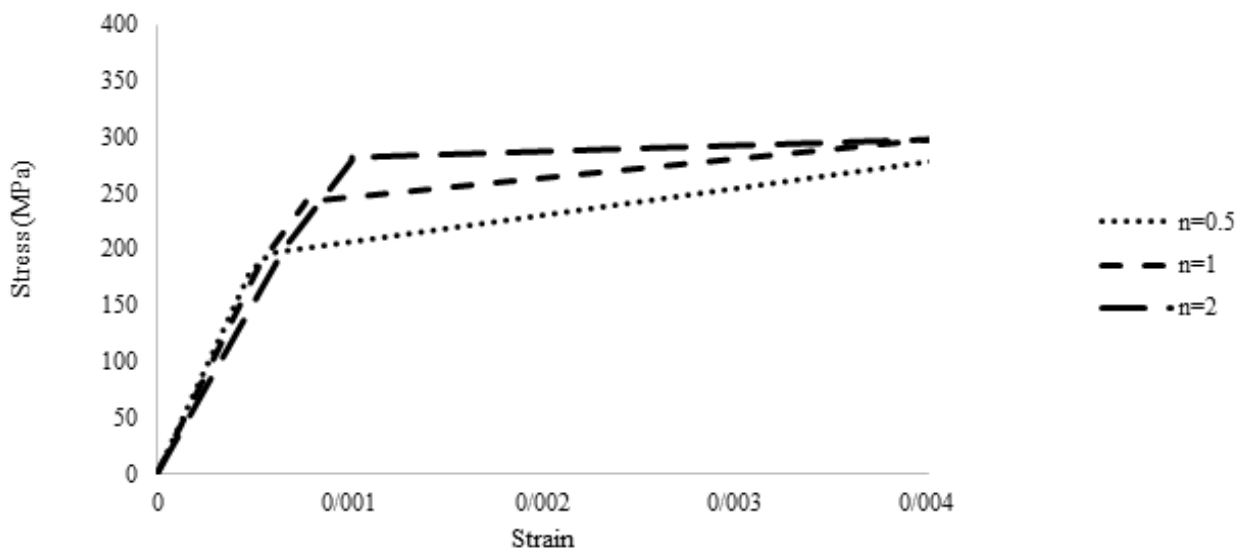
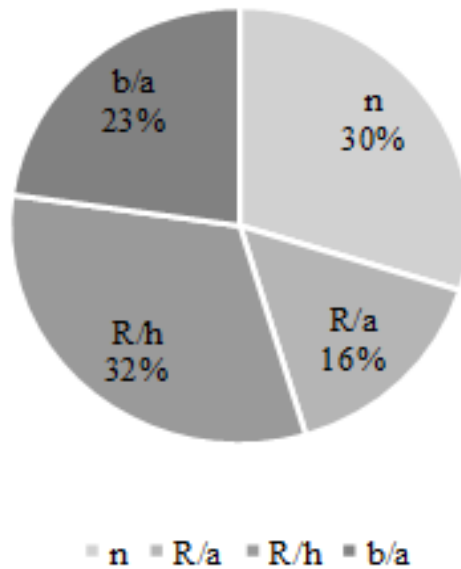


Fig. 26. The stress-strain curve of the single curved FGM shell under impact load (Friedlander).

**Table 5. The coefficient of determination of the geometrical and mechanical parameters of the single curved FGM shell.**

Parameters	$x_i$	$y_i$	$r$	Parameters	$x_i$	$y_i$	$r$
$n$	0.2	-0.0445	0.907	$R/a$	0.8	-0.0010	0.475
	0.33	-0.0491			1.33	-0.0036	
	0.5	-0.0542			2	-0.0165	
	1	-0.0658			4	-0.0658	
	2	-0.0803			8	-0.0664	
	3	-0.0886			12	-0.0637	
$R/h$	5	-0.0987	0.971	$b/a$	20	-0.0609	0.693
	60	-0.0004			0.2	-0.0020	
	100	-0.0012			0.33	-0.0123	
	150	-0.0032			0.5	-0.0226	
	300	-0.0352			1	-0.0658	
	600	-0.0657			2	-0.1105	
	900	-0.0902			3	-0.1077	
1500	-0.1312	5	-0.1082				



**Fig. 27. The effect of each parameters on the maximum displacement of the single curved FGM shell.**

**8- Conclusions**

The present study was conducted to analyze the elasto-plastic behavior and the effect of mechanical and geometrical properties of the single curved FGM shells under impact load. The results of the nonlinear dynamic response for single curved FGM shells are summarized as follows:

-In order to evaluate the effect of mechanical properties on the shell, the volume fraction index has been considered. The maximum displacement of the shell was increased by increasing the volume fraction index, in such a way that the

maximum displacement occurred in the metal-rich shell ( $n = \infty$ ) and the minimum displacement occurred in the ceramic-rich shell ( $n = 0$ ). The response of the other shells lay between these two extreme cases. Also, by increasing the volume fraction index, the maximum displacement location moves toward the shell's center.

-By evaluating the geometrical properties of the single curved FGM shell, the maximum displacement of the shell was decreased by increasing the thickness ratio. Also by increasing the aspect ratio, the maximum displacement of the

shell was increased and by increasing the curvature radius, the maximum displacement of the shell at first has increased and then decreased. The value of each geometrical property of the shell affects the location of the maximum displacement so that by decreasing the thickness ratio, aspect ratio. and curvature radius, the maximum displacement location moves toward the shell's center.

-After considering the effect of mechanical and geometrical properties of the shell on the maximum displacement, it was observed that the thickness ratio with the largest coefficient of determination had the greatest effect on the shell response.

-According to the results, it can be seen that the elasto-plastic response of FGM shells is similar to the response of the homogeneous shells. Therefore, the TTO model can be used to describe the mechanical behavior of the FGM shells beyond the elastic region, which governs the FGM response based on the plastic region of the metal phase

## 9- Nomenclature

### English symbols

$a$	Span of shell, m
$b$	Length of shell, m
$h$	Thickness of shell, m
$R$	Radius of shell, m
$n$	Volume fraction index
$P$	Material properties
$V$	Volume fractions
$E$	Modulus of elasticity, GPa
$r$	Coefficient of determination
$q$	Parameter transfer

### Subscript

$c$	Ceramic
$m$	Metal
$\circ$	Yield of the metal
$y$	Yield of the FGM

### Greek symbols

$\nu$	Poisson ratio
$\rho$	Density, kg/m <sup>3</sup>
$\kappa$	Curvature, 1/m
$\sigma$	Stress
$\varepsilon$	Strain

## References

- [1] H. Yin, L. Sun, and G. H. Paulino, "Micromechanics-based elastic model for functionally graded materials with particle interactions," *Acta Materialia*, vol. 52, no. 12, pp. 3535-3543, 2004.
- [2] D. L. Christy, T. M. Pillai, and P. Nagarajan, "Thin plate element for applied element method," in *Structures*, vol. 22: Elsevier, pp. 1-12, 2019.
- [3] S. Ashok and P. Jeyaraj, "Static deflection and thermal stress analysis of non-uniformly heated tapered composite laminate plates with ply drop-off," in *Structures*, vol. 15: Elsevier, pp. 307-319, 2018.
- [4] M. Bever and P. Duwez, "Gradients in composite materials," *Materials Science and Engineering*, vol. 10, pp. 1-8, 1972.
- [5] M. Koizumi, "FGM activities in Japan," *Composites Part B: Engineering*, vol. 28, no. 1-2, pp. 1-4, 1997.
- [6] Mojtaba Shahraki, Farzad Shahabian, Reza jome manzari "Free vibration analysis of FGM plates with Opening and Stiffener", *Amirkabir Journal of Civil Engineering*, Published Online, Iran, 2019, (in Persian).
- [7] R. Sridhar and D. R. Prasad, "Damage assessment of functionally graded reinforced concrete beams using hybrid fiber engineered cementitious composites," in *Structures*, vol. 20: Elsevier, pp. 832-847, 2019.
- [8] C. Horgan and A. Chan, "The pressurized hollow cylinder or disk problem for functionally graded isotropic linearly elastic materials," *Journal of Elasticity*, vol. 55, no. 1, pp. 43-59, 1999.
- [9] Mojtaba Shahraki, Farzad Shahabian, Reza jome manzari "Effect of Opening and Stiffener on Geometric Nonlinear Dynamical Behavior of Single-Curved FGM Shells under the Blast Loads", *Amirkabir Journal of Civil Engineering*, Published Online, Iran, 2018, (in Persian).
- [10] D. K. Nguyen, K. V. Nguyen, B. S. Gan, and S. Alexandrov, "Nonlinear bending of elastoplastic functionally graded ceramic-metal beams subjected to nonuniform distributed loads," *Applied Mathematics and Computation*, vol. 333, pp. 443-459, 2018.
- [11] G. Nie and Z. Zhong, "Exact solutions for elastoplastic stress distribution in functionally graded curved beams subjected to pure bending," *Mechanics of Advanced Materials and Structures*, vol. 19, no. 6, pp. 474-484, 2012.
- [12] D. Y. Gao et al., *Advances in mechanics and mathematics*. Springer, 2003.
- [13] M. Bocciarelli, G. Bolzon, and G. Maier, "A constitutive model of metal-ceramic functionally graded material behavior: formulation and parameter identification," *Computational Materials Science*, vol. 43, no. 1, pp. 16-26, 2008.
- [14] T. Nakamura, T. Wang, and S. Sampath, "Determination of properties of graded materials by inverse analysis and instrumented indentation," *Acta Materialia*, vol. 48, no. 17, pp. 4293-4306, 2000.
- [15] Y. Shabana, N. Noda, and K. Tohgo, "Elasto-plastic thermal stresses in functionally graded materials considering microstructure effects," in *Current Advances in Mechanical Design and Production VII: Elsevier*, pp. 223-231, 2000.
- [16] A. Ozturk and M. Gulgec, "Elastic-plastic stress analysis in a long functionally graded solid cylinder with fixed ends subjected to uniform heat generation," *International Journal of Engineering Science*, vol. 49, no. 10, pp. 1047-

- 1061, 2011.
- [17] V. Tvergaard, "Theoretical investigation of the effect of plasticity on crack growth along a functionally graded region between dissimilar elastic-plastic solids," *Engineering Fracture Mechanics*, vol. 69, no. 14-16, pp. 1635-1645, 2002.
- [18] Z. H. Jin, G. H. Paulino, and R. H. Dodds Jr, "Cohesive fracture modeling of elastic-plastic crack growth in functionally graded materials," *Engineering Fracture Mechanics*, vol. 70, no. 14, pp. 1885-1912, 2003.
- [19] Q. Xu and Z. Lu, "An elastic-plastic cohesive zone model for metal-ceramic interfaces at finite deformations," *International Journal of Plasticity*, vol. 41, pp. 147-164, 2013.
- [20] R. Gunes, M. Aydin, M. K. Apalak, and J. Reddy, "The elasto-plastic impact analysis of functionally graded circular plates under low-velocities," *Composite Structures*, vol. 93, no. 2, pp. 860-869, 2011.
- [21] T. Hause, "Advanced functionally graded plate-type structures impacted by blast loading," *International Journal of Impact Engineering*, vol. 38, no. 5, pp. 314-321, 2011.
- [22] C. Loy, K. Lam, and J. Reddy, "Vibration of functionally graded cylindrical shells," *International Journal of Mechanical Sciences*, vol. 41, no. 3, pp. 309-324, 1999.
- [23] C. Aksoylar, A. Ömercikoğlu, Z. Mecitoğlu, and M. H. Omurtag, "Nonlinear transient analysis of FGM and FML plates under blast loads by experimental and mixed FE methods," *Composite Structures*, vol. 94, no. 2, pp. 731-744, 2012.
- [24] R. Williamson, B. Rabin, and J. Drake, "Finite element analysis of thermal residual stresses at graded ceramic-metal interfaces. Part I. Model description and geometrical effects," *Journal of Applied Physics*, vol. 74, no. 2, pp. 1310-1320, 1993.
- [25] M. Bhattacharyya, S. Kapuria, and A. Kumar, "On the stress to strain transfer ratio and elastic deflection behavior for Al/SiC functionally graded material," *Mechanics of Advanced Materials and Structures*, vol. 14, no. 4, pp. 295-302, 2007.
- [26] S. Abrate, "Functionally graded plates behave like homogeneous plates," *Composites part B: engineering*, vol. 39, no. 1, pp. 151-158, 2008.
- [27] A. Hajlaoui, E. Triki, A. Frikha, M. Wali, and F. Dammak, "Nonlinear dynamics analysis of FGM shell structures with a higher order shear strain enhanced solid-shell element," *Latin American Journal of Solids and Structures*, vol. 14, no. 1, pp. 72-91, 2017.
- [28] A. S. Nowak and K. R. Collins, *Reliability of structures*. CRC Press, 2012.

#### HOW TO CITE THIS ARTICLE

M. Shahraki, F. Shahabian, M. Koohestani, The nonlinear dynamic analysis of elasto-plastic behaviour of the single-curved FGM shells under impact load, *AUT J. Civil Eng.*, 5(1) (2021) 17-36

DOI: [10.22060/ajce.2020.17389.5627](https://doi.org/10.22060/ajce.2020.17389.5627)



